

Article

# Tuning Parameters of the Fractional Order PID-LQR Controller for Semi-Active Suspension

Jin Gao \* and Hui Li

Faculty of Transportation Engineering, Kunming University of Science and Technology, Kunming 650500, China; 20212206097@stu.kust.edu.cn

\* Correspondence: gaojin@kust.edu.cn

**Abstract:** In order to further improve the control effect of proportion integral differential (PID) control and linear quadratic regulator (LQR) control, and improve vehicle ride comfort and enhance body stability, the 7 DOF semi-active suspension model was established, and the fractional order  $PI^\lambda D^\mu$ -LQR controller was designed by combining fractional order  $PI^\lambda D^\mu$  control theory and LQR control theory. The semi-active suspension model in this paper is more complex, and there are many parameters in the controller. The optimal weighting coefficient of 12 vehicle smoothness evaluation indicators and parameters  $K_p$ ,  $K_i$ ,  $K_d$ ,  $\lambda$  and  $\mu$  in the controller were founded by NSGA-II algorithm. After optimization, the optimized parameters were brought into the controller for random pavement simulation. Compared to the traditional passive suspension, fractional order  $PI^\lambda D^\mu$  individual control and LQR separate control, the simulation results show that the effect of fractional order  $PI^\lambda D^\mu$ -LQR control is very significant. The evaluation index of vehicle smoothness has been significantly improved, and the use of fractional order  $PI^\lambda D^\mu$ -LQR control has significantly improved the working performance of the suspension and improved the smoothness of the vehicle. At the same time, the adjusting force output of the actuator is very balanced, which inhibits the roll of the body and improves the anti-roll performance. After simulation, the excellent performance of the designed fractional  $PI^\lambda D^\mu$ -LQR controller was verified, and the introduced NSGA-II algorithm played an important role in the controller parameter tuning work, which shows that the fractional order  $PI^\lambda D^\mu$ -LQR controller and NSGA-II algorithm cooperate with each other to achieve good control effects.



**Citation:** Gao, J.; Li, H. Tuning Parameters of the Fractional Order PID-LQR Controller for Semi-Active Suspension. *Electronics* **2023**, *12*, 4115. <https://doi.org/10.3390/electronics12194115>

Academic Editor: Mahmut Reyhanoglu

Received: 1 September 2023  
Revised: 29 September 2023  
Accepted: 29 September 2023  
Published: 1 October 2023



**Copyright:** © 2023 by the authors. Licensee MDPI, Basel, Switzerland. This article is an open access article distributed under the terms and conditions of the Creative Commons Attribution (CC BY) license (<https://creativecommons.org/licenses/by/4.0/>).

**Keywords:**  $PI^\lambda D^\mu$  control; LQR control; fractional order  $PI^\lambda D^\mu$ -LQR control; NSGA-II algorithm; actuator adjusting force

## 1. Introduction

The research frontier for intelligent semi-active suspensions is the design of the controller, and many researchers are committed to developing a semi-active suspension controller with excellent performance to improve the working performance of the suspension and improve the smoothness of the vehicle. Ref. [1] established a 1/4 semi-active suspension model and designed a controller based on deep reinforcement learning. Based on state feedback and pre-aim feed-forward, a controller for state feedback and pre-sight-forward feed-forward was designed by [2]. Ref. [3] designed a semi-active suspension based on hydropneumatic mechanism and a semi-active suspension controller with a linear quadratic gaussian (LQG) optimal control algorithm. Ref. [4] developed a cloud-based parameter-adjustable adaptive semi-active suspension control method, while AMESim software was used by [5] to model the Continuous Damping Control damper adjustable damping shock absorber, analyze the dynamics of a 2-DOF semi-active suspension, and propose a genetic algorithm to improve the fuzzy rule. The control effect of the semi-active suspension controller depends largely on the parameters in the controller; for example, the control effect of the LQR controller depends on the weighting coefficient of various

performance indicators, the performance of the PID controller mainly depends on  $K_p$ ,  $K_i$  and  $K_d$  parameters, and the control effect of the fuzzy controller depends on the fuzzy rules formulated, so the key to the design of the controller is the tuning of the controller parameters. For this reason, many scholars have conducted research on the tuning of parameters in the controller, and proposed different parameter tuning methods for different control modes. Ref. [6] proposed a locust optimization algorithm (GOA) and used it to adjust the parameters in the PID controller. Ref. [7] used the artificial fish swarm algorithm (AFSA) to determine the weighting coefficient in the LQR controller. Ref. [8] designed the semi-active suspension fuzzy controller and formulated the fuzzy rules of the controller, while [9] combined fuzzy control algorithm and particle swarm optimization algorithm to adjust P, I, D parameters.

The parameter adjustment in the suspension controller is highly dependent on the algorithm, and the appropriate optimization algorithm can not only improve the control effect of the controller, but also greatly improve the comfort and driving smoothness of the car. Different suspension controllers have been designed which use particle swarm algorithm, fuzzy control algorithm, deep learning algorithm, etc. to adjust the parameters in the controller, which also have good control effects [6–9]. In fact, according to the “no free lunch” (NFL) theorem, for the same optimization problem, in the limited search space, different optimization algorithms can achieve different optimization effects, and no other algorithm can be better than the linear enumeration method of the search space or the pure random search algorithm [10,11]. Orosz et al. [12] also mentioned that due to the “no free lunch” theorem of mathematical optimization, no one evolutionary optimization algorithm can outperform the others if all possible problems are averaged, and their article outlines the optimization techniques widely used in electric motors, summarizing the challenges and open problems of robust design optimization in applications and the development prospects of emerging technologies.

The NSGA-II algorithm belongs to a pure random search algorithm, whose principle is to imitate the “survival of the fittest” law of nature, with a strong gradient search ability. Although the NSGA-II algorithm is not universal to all optimization problems, for the semi-active suspension control system parameter optimization problem, it has a good optimization effect, which can be verified from the work of other researchers. For example, [13] constructed a rigid-flex coupling vehicle model of flexible control arm and torsion beam for vehicle dynamics simulation. The optimization goal is to control the total weight of the arm and torsion beam, ride comfort and handling stability performance indicators. Fatigue life, stiffness and modal frequency of control arms and torsion beams were used as constraints. Then, the NSGA-II was used to perform multi-objective optimization of the control arm and torsion beam to determine the lightweight scheme. Ref. [14] proposed to optimize the fuzzy logic controller (FLC) active seat suspension applied to articulated truck semi-trailer seats by using the NSGA-II algorithm, and the two objective functions optimized are seat vertical acceleration and controller control force to improve the seating comfort. Ref. [15] established a 1/4 semi-active suspension model and proposed to optimize spring rate and suspension damping by using the NSGA-II algorithm to improve vehicle comfort and ride.

The suspension model established by [13–15] is mainly a relatively simple 1/4 suspension model; the 1/4 suspension model can only consider the suspension performance indicators at a single axle, and it is difficult to comprehensively evaluate the performance of the whole vehicle, whereas the full vehicle model can take into account the force and movement of the vertical, pitch, roll and other degrees of freedom during the driving process of the car, optimize more indicators, evaluate the vehicle more comprehensively, and be more conducive to the study of the smoothness of the car. Secondly, because fractional order  $PI^\lambda D^\mu$  control has higher design freedom, the design of fractional order  $PI^\lambda D^\mu$  controller is more flexible than integer order PID controller [16,17]. Therefore, according to the fractional order  $PI^\lambda D^\mu$  control theory and LQR control theory, a better fractional order  $PI^\lambda D^\mu$ -LQR controller is designed. Finally, the NSGA-II algorithm is improved on the basis of the traditional genetic algorithm (GA) and the first generation of non-dominated ranking

genetic algorithm (NSGA), which overcomes many shortcomings of the traditional algorithm and is especially suitable for solving complex multi-objective optimization problems. The semi-active suspension system in this paper belongs to a very complex multi-objective optimization problem. Moreover, in the above literature, the two-dimensional plane representation method was used to explain the concepts of non-dominated sorting and crowding sorting of NSGA-II. For the case of many optimization goals, the concept of non-dominated sorting and crowding sorting is explained better by the three-dimensional spatial representation method, and the three-dimensional spatial solution is obtained, which is easier to understand and more clearly illustrates the problem. Therefore, this paper applies the NSGA-II algorithm to the semi-active suspension control system to solve the parameter tuning problem of the semi-active suspension fractional order  $PI^\lambda D^\mu$ -LQR controller.

In summary, the 7-DOF semi-active suspension model is established, and the fractional order  $PI^\lambda D^\mu$  control theory and LQR control theory are combined to design the fractional order  $PI^\lambda D^\mu$ -LQR composite controller. The NSGA-II algorithm is used to find the optimal performance indicator weighting coefficient and optimal parameter  $K_p$ ,  $K_i$  and  $K_d$ ,  $\lambda$  and  $\mu$  in the fractional-order  $PI^\lambda D^\mu$ -LQR controller.

## 2. Building the Mathematical Model of the Control System

### 2.1. Mathematical Model of Semi-Active Suspension

Taking the center of mass of the vehicle as the coordinate origin, the vehicle coordinate system is established with the longitude, lateral and vertical directions of the vehicle as the X axis, Y axis and Z axis, respectively, as shown in Figure 1. The vertical displacement of the body occurs along the Z axis, rotation around the Y axis is the pitch, rotation around the X axis is the roll, and the vertical displacement of the four unsprung masses along the Z axis are taken as the 7 DOF in the process of vehicle driving.

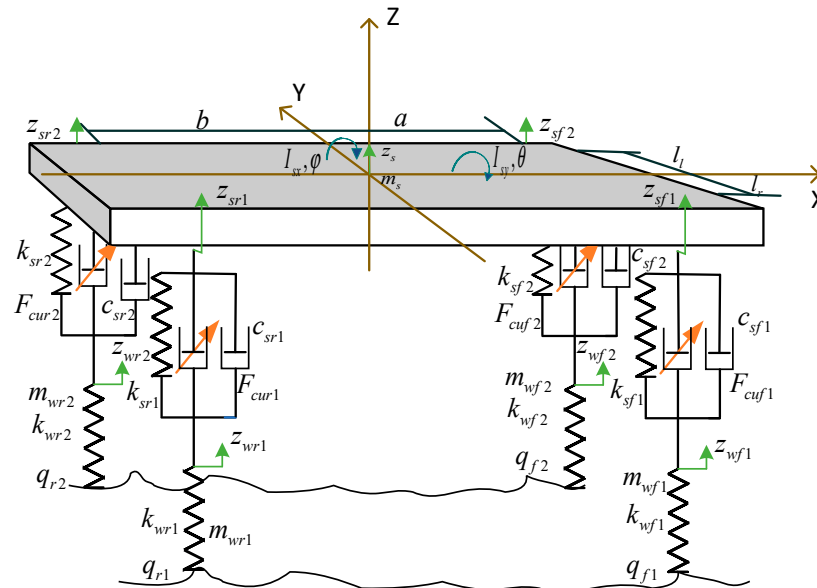


Figure 1. Seven degrees of freedom dynamic model of semi-active suspension.

In Figure 1,  $z_s$  is the vertical displacement of the body center of mass;  $\varphi$  and  $\theta$  represent the body pitch angle and the body roll angle, respectively;  $m_{wf1}$ ,  $m_{wf2}$ ,  $m_{wr1}$ ,  $m_{wr2}$  represent the vehicle unsprung mass of the right front, left front, left rear and right rear, respectively;  $k_{wf1}$ ,  $k_{wf2}$ ,  $k_{wr1}$ ,  $k_{wr2}$  represent the stiffness coefficients of right front tire, left front tire, right rear tire and left rear tire, respectively;  $k_{sf1}$ ,  $k_{sf2}$ ,  $k_{sr1}$ ,  $k_{sr2}$  represent the stiffness coefficients of right front suspension, left front suspension, right rear suspension and left rear suspension coefficient, respectively;  $c_{sf1}$ ,  $c_{sf2}$ ,  $c_{sr1}$ ,  $c_{sr2}$  represent the damping coefficient of right front suspension, left front suspension, right rear suspension and left rear suspension, respectively;  $q_{f1}$ ,  $q_{f2}$ ,  $q_{r1}$ ,  $q_{r2}$  represent the vertical displacement of the road input to the

four wheels;  $z_{wf1}, z_{wf2}, z_{wr1}, z_{wr2}$  represent the vertical displacement of the four wheels;  $z_{sf1}, z_{sf2}, z_{sr1}, z_{sr2}$  represent the vertical displacement of the body above the four wheels;  $F_{wf1}, F_{wf2}, F_{wr1}, F_{wr2}$  represent the right front suspension, left front suspension, right rear suspension and left rear suspension output force, respectively;  $a, b$  is the distance from the body center of mass to the front and rear wheel axle;  $L_l, L_r$  is the distance from the body center of mass to the center lines of the left and right wheel, respectively. The vehicle mass is expressed as  $m_s$ , the pitch moment of inertia is expressed as  $I_{sy}$ , the roll moment of inertia is expressed as  $I_{sx}$ , the road roughness coefficient is expressed as  $G_0$ , the experimental vehicle speed is expressed as  $u$ , and the lower stop frequency is expressed as  $f_0$ .

By analyzing the force and moment of the vehicle's sprung and unsprung masses, the following differential equations of motion can be established [18–21]:

The balance equation of the Z axis vertical force at the center of mass of the body is shown in Formula (1):

$$m_s \ddot{z}_s = k_{sf1}(z_{wf1} - z_{sf1}) + c_{sf1}(\dot{z}_{wf1} - \dot{z}_{sf1}) + k_{sf2}(z_{wf2} - z_{sf2}) + c_{sf2}(\dot{z}_{wf2} - \dot{z}_{sf2}) + k_{sr1}(z_{wr1} - z_{sr1}) + c_{sr1}(\dot{z}_{wr1} - \dot{z}_{sr1}) + k_{sr2}(z_{wr2} - z_{sr2}) + c_{sr2}(\dot{z}_{wr2} - \dot{z}_{sr2}) + F_{cuf1} + F_{cuf2} + F_{cur1} + F_{cur2} \tag{1}$$

The body pitching torque balance equation is shown in Formula (2):

$$I_{sy} \ddot{\phi} = b[k_{sr1}(z_{wr1} - z_{sr1}) + c_{sr1}(\dot{z}_{wr1} - \dot{z}_{sr1}) + k_{sr2}(z_{wr2} - z_{sr2}) + c_{sr2}(\dot{z}_{wr2} - \dot{z}_{sr2})] + F_{cur1} + F_{cur2} - a[k_{sf1}(z_{wf1} - z_{sf1}) + c_{sf1}(\dot{z}_{wf1} - \dot{z}_{sf1}) + k_{sf2}(z_{wf2} - z_{sf2}) + c_{sf2}(\dot{z}_{wf2} - \dot{z}_{sf2})] + F_{cuf1} + F_{cuf2} \tag{2}$$

The body roll moment balance equation is shown in Formula (3):

$$I_{sx} \ddot{\theta} = L_l[k_{sf2}(z_{wf2} - z_{sf2}) + c_{sf2}(\dot{z}_{wf2} - \dot{z}_{sf2}) + k_{sr2}(z_{wr2} - z_{sr2}) + c_{sr2}(\dot{z}_{wr2} - \dot{z}_{sr2})] + F_{cuf2} + F_{cur2} - L_r[k_{sf1}(z_{wf1} - z_{sf1}) + c_{sf1}(\dot{z}_{wf1} - \dot{z}_{sf1}) + k_{sr1}(z_{wr1} - z_{sr1}) + c_{sr1}(\dot{z}_{wr1} - \dot{z}_{sr1})] + F_{cuf1} + F_{cur1} \tag{3}$$

Four unsprung mass vertical force balance equations are shown in Formula (4):

$$\begin{cases} m_{wf1} \ddot{z}_{wf1} = k_{wf1}(q_{f1} - z_{wf1}) - k_{sf1}(z_{wf1} - z_{sf1}) - c_{sf1}(\dot{z}_{wf1} - \dot{z}_{sf1}) - F_{cuf1} \\ m_{wf2} \ddot{z}_{wf2} = k_{wf2}(q_{f2} - z_{wf2}) - k_{sf2}(z_{wf2} - z_{sf2}) - c_{sf2}(\dot{z}_{wf2} - \dot{z}_{sf2}) - F_{cuf2} \\ m_{wr1} \ddot{z}_{wr1} = k_{wr1}(q_{r1} - z_{wr1}) - k_{sr1}(z_{wr1} - z_{sr1}) - c_{sr1}(\dot{z}_{wr1} - \dot{z}_{sr1}) - F_{cur1} \\ m_{wr2} \ddot{z}_{wr2} = k_{wr2}(q_{r2} - z_{wr2}) - k_{sr2}(z_{wr2} - z_{sr2}) - c_{sr2}(\dot{z}_{wr2} - \dot{z}_{sr2}) - F_{cur2} \end{cases} \tag{4}$$

When the variation range of body pitch angle and roll angle is small enough, the displacement of the suspension mass endpoints above the four wheels can be expressed as Formula (5):

$$\begin{cases} z_{sf1} = z_s - L_r \theta - a \phi \\ z_{sf2} = z_s - L_l \theta - a \phi \\ z_{sr1} = z_s - L_r \theta + b \phi \\ z_{sr2} = z_s + L_l \theta + b \phi \end{cases} \tag{5}$$

The state space expression (6) can be obtained by combining the above Formulas (1)–(5):

$$\begin{cases} \dot{X} = AX + BU + EW \\ Y = CX + DU \end{cases} \quad (6)$$

In Formula (6), matrix  $A$  is the system matrix, matrix  $B$  is the control matrix, matrix  $C$  is the output matrix, matrix  $D$  is the transfer matrix, matrix  $E$  is the disturbance matrix,  $X$  is the state variable,  $Y$  is the output variable,  $U$  is the control variable, and  $W$  is the perturbation variable.

A total of 18 variables including body vertical displacement, body pitch angle, body roll angle, vertical displacement of four unsprung masses, road input at four wheels, body vertical speed, body pitch angle speed, body roll angle speed and four vertical speeds of unsprung masses are selected as the state variation of the system, namely:

$$X = (z_s, \phi, \theta, z_{wf1}, z_{wf2}, z_{wr1}, z_{wr2}, q_{f1}, q_{f2}, q_{r1}, q_{r2}, \dot{z}_s, \dot{\phi}, \dot{\theta}, \dot{z}_{wf1}, \dot{z}_{wf2}, \dot{z}_{wr1}, \dot{z}_{wr2})^T \quad (7)$$

A total of 11 variables including body vertical acceleration, body pitch angle acceleration, body roll angle acceleration, four suspension dynamic travel variables and four tire dynamic displacement variables are selected as the output variables of the system, namely:

$$Y = (\ddot{z}_s, \ddot{\phi}, \ddot{\theta}, z_{swf1}, z_{swf2}, z_{swr1}, z_{swr2}, z_{qwf1}, z_{qwf2}, z_{qwr1}, z_{qwr2})^T \quad (8)$$

Four damping adjustment force variables,  $F_{cuf1}, F_{cuf2}, F_{cur1}, F_{cur2}$ , are selected as the components of the control vector  $U$ , namely:

$$U = (F_{cuf1}, F_{cuf2}, F_{cur1}, F_{cur2})^T \quad (9)$$

The vertical speed of the road surface at the four wheels,  $\dot{q}_{f1}, \dot{q}_{f2}, \dot{q}_{r1}, \dot{q}_{r2}$ , was selected as the component of the disturbance vector  $W$ , namely:

$$W = (\dot{q}_{f1}, \dot{q}_{f2}, \dot{q}_{r1}, \dot{q}_{r2})^T \quad (10)$$

### 2.2. Pavement Simulation Model

The filtered white noise input is used as the pavement simulation model, and the time-domain expression of the vertical speed of the pavement is shown in Formula (11):

$$\begin{cases} \dot{q}_{f1} = -2\pi f_0 q_{f1} + 2\pi\sqrt{G_0}uw_1 \\ \dot{q}_{f2} = -2\pi f_0 q_{f2} + 2\pi\sqrt{G_0}uw_2 \\ \dot{q}_{r1} = -2\pi f_0 q_{r1} + 2\pi\sqrt{G_0}uw_3 \\ \dot{q}_{r2} = -2\pi f_0 q_{r2} + 2\pi\sqrt{G_0}uw_4 \end{cases} \quad (11)$$

where  $w_1, w_2, w_3, w_4$  is the unit Gaussian white noise with an average value of 0 and an intensity of 1, which can be directly invoked from the library when building the simulation model with Simulink. The pavement model established by Simulink is shown in Figure 2.

In Figure 2,  $G_0$  represents the pavement unevenness coefficient of class B,  $u$  represents the speed of the vehicle,  $f_0$  represents the frequency under the pavement,  $q_{f1}(t)$  represents the vertical displacement of the road surface of the front wheel,  $\dot{q}_{f1}$  represents the vertical speed of the road surface of the front wheel, and  $w_1$  is the Gaussian white noise input to the front wheel road.

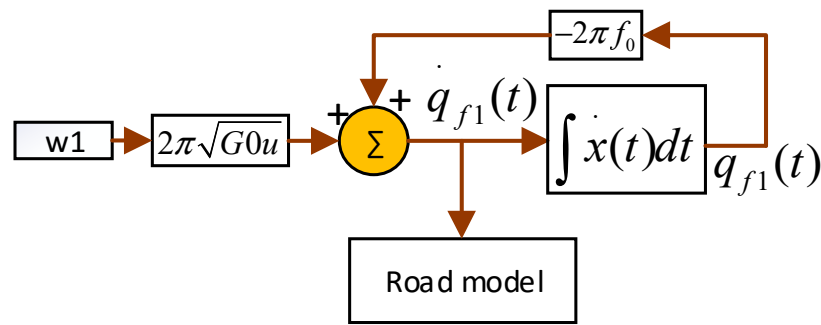


Figure 2. Pavement model of front wheel 1.

Since the road conditions at each wheel of the vehicle do not differ much during the driving process, the road model at the four wheels is the same as that at the front wheel 1. According to the harmonic superposition method, references [22,23], a B class 3D road model with a length of 400 m and a width of 4 m is established as shown in Figure 3.

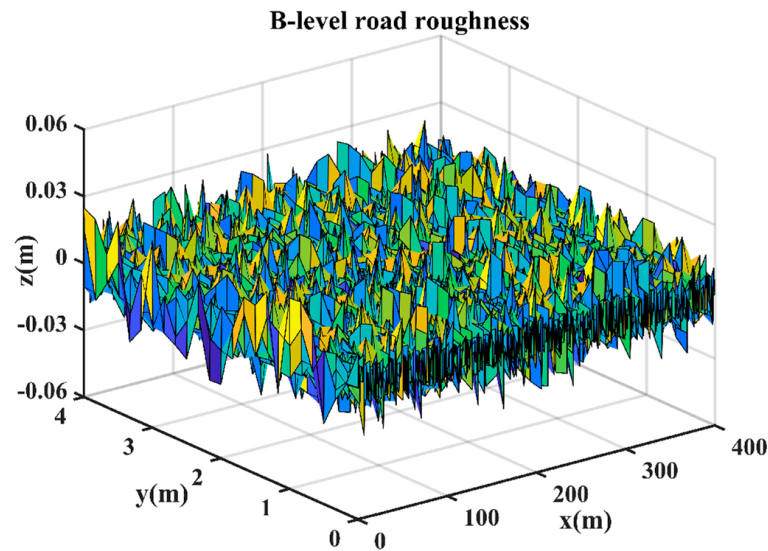


Figure 3. B Class 3D road model.

$x$ ,  $y$  and  $z$  in Figure 3 are the length, width and rough surface thickness of the 3D road, respectively.

### 3. Designing the Fractional Order $PI^\lambda D^\mu$ -LQR Controller

#### 3.1. Fractional Order $PI^\lambda D^\mu$ Controller

Fractional order  $PI^\lambda D^\mu$  control is error control. In the vehicle driving process, the vehicle indicator people are most concerned about is the comfort of the body. Thus, the body vertical acceleration as the control object of fractional order  $PI^\lambda D^\mu$  control, and 0 as the expected value can achieve good control effect, with the actual output value of the body vertical acceleration as feedback. The difference between the feedback value and the expected value of the body’s vertical acceleration is used as the error signal. The control principle of fractional order  $PI^\lambda D^\mu$  control is as follows [24] (12):

$$U_{PI^\lambda D^\mu}(t) = K_p e(t) + K_i D^{-\lambda} e(t) + K_d D^\mu e(t) \tag{12}$$

In Formula (12),  $e(t)$  is the error signal,  $U_{PI^\lambda D^\mu}(t)$  is the output of the fractional order  $PI^\lambda D^\mu$  controller,  $K_p$  is the scale coefficient,  $K_i$  is the integral coefficient,  $K_d$  is the differential coefficient,  $\lambda$  is the integral order, and  $\mu$  is the differential order, where the  $\lambda$  and  $\mu$  can be any real number.

The basic structure block diagram of a fractional order  $PI^\lambda D^\mu$  controller is shown in Figure 4.

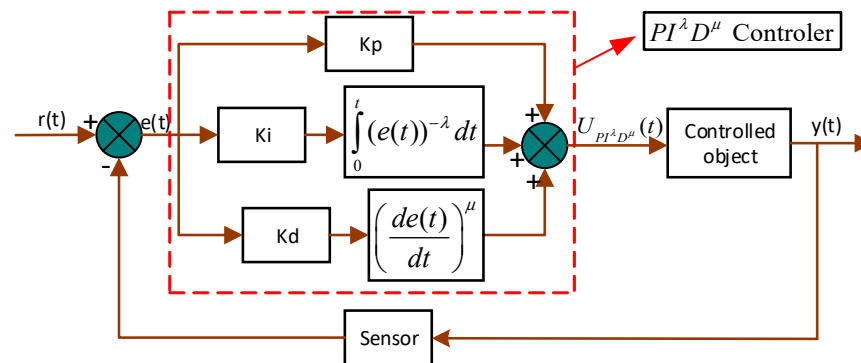


Figure 4. Structure block diagram of fractional order  $PI^\lambda D^\mu$  controller.

The fractional order  $PI^\lambda D^\mu$  control principle in Figure 4 is described as using the corresponding sensor of the vehicle to obtain the output variable  $y(t)$ , and the error signal  $e(t)$  between the expected value  $r(t)$  and the output variable  $y(t)$  is used as the input of the fractional order  $PI^\lambda D^\mu$  controller as the output of the controller. Fractional order  $PI^\lambda D^\mu$  control extends integer integration and differentiation to fractional order when performing integration operations and differential operations, and the parameter adjustment is more flexible, which is better than the traditional integer order PID control method.

Parameter  $K_p$  can adjust the rise time and adjustment time of the system, mainly affecting the response speed of the system, parameter  $K_i$ ;  $\lambda$  can adjust the overshoot of the system, mainly affecting the adjustment accuracy of the system, parameter  $K_d$ ;  $\mu$  can adjust the number of oscillations of the system, mainly affecting the severity of the oscillation of the system. With reference to [25], the fractional order  $PI^\lambda D^\mu$  controller is designed according to the Oustaloup algorithm.

### 3.2. LQR Controller

The 18 vehicle state variables in Formula (7) are taken as the feedback signals of the LQR controller. The controller uses the feedback signals as a reference to issue control instructions to the actuator, and the actuator outputs appropriate adjusting force. The control principle of LQR control is shown in Formula (13):

$$U_{LQR}(t) = -KX(t) \tag{13}$$

where  $U_{LQR}(t)$  is the output of the LQR controller, and  $K$  is the gain of the controller. Gain  $K$  can be obtained from the following formula:

$$K = R_d^{-1}B^T P \tag{14}$$

$P$  is obtained from the following Riccati equation:

$$A^T P + PA - PBR_d^{-1}B^T P + Q_d = 0 \tag{15}$$

Formulas (13) and (14) can be solved using MATLAB commands:  $[k, p] = lqr(A, B, Q_d, R_d, N_d)$ , where:

$$\begin{aligned} Q_d &= C^T Q C; \\ N_d &= C^T Q D; \\ R_d &= R + D^T Q D \end{aligned} \tag{16}$$

In Formula (16),  $Q$  is the weight matrix of 11 performance indicators, and  $R$  is the weight matrix of four actuator regulating forces, respectively expressed as follows:

$$Q = \text{diag}(q_1, q_2, q_3, q_4, q_5, q_6, q_7, q_8, q_9, q_{10}, q_{11})$$

$$R = \text{diag}(q_{12}, q_{12}, q_{12}, q_{12})$$
(17)

where:  $q_1$  is the weighting coefficient of vertical acceleration at the body center of mass,  $q_2$  is the weighting coefficient of pitch angle acceleration,  $q_3$  is the weighting coefficient of roll angle acceleration,  $q_4, q_5, q_6, q_7$  are the weighting coefficients of four suspension dynamic travel variables,  $q_8, q_9, q_{10}, q_{11}$  are the weighting coefficients of four wheel dynamic displacement variables, and  $q_{12}$  is the weighting coefficient of four actuator output forces.

### 3.3. Fractional Order $PI^\lambda D^\mu$ -LQR Controller

The fractional order  $PI^\lambda D^\mu$  controller and the LQR controller are integrated into the fractional order  $PI^\lambda D^\mu$ -LQR controller, and the control model is shown in Figure 5.

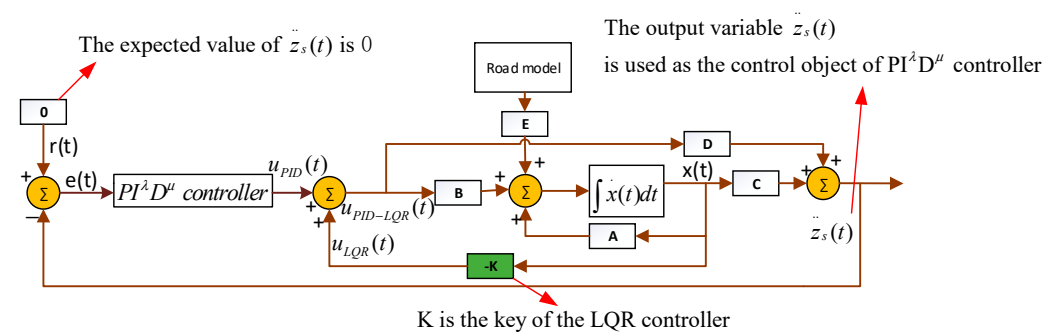


Figure 5. Simulation model of semi-active suspension system.

Figure 5 is the core of the entire control system. The fractional order  $PI^\lambda D^\mu$ -LQR controller is composed of the fractional order  $PI^\lambda D^\mu$  controller and the LQR controller, wherein the expected value  $r(t) = 0$  of the fractional order  $PI^\lambda D^\mu$  control, the controlled object is the vertical acceleration of the body, and  $K$  is the optimal feedback gain of the LQR controller.

The control principle of the fractional order  $PI^\lambda D^\mu$ -LQR controller is as follows [26,27] (18):

$$U_{PI^\lambda D^\mu-LQR}(t) = U_{PID}(t) + U_{LQR}(t)$$
(18)

where  $U_{PI^\lambda D^\mu-LQR}(t)$  is the comprehensive regulating force of the four actuators.

## 4. NSGA-II Algorithm Optimizes the Fractional-Order $PI^\lambda D^\mu$ -LQR Controller Parameters

### 4.1. Designing the Objective Function

The process of finding an optimal solution is almost entirely dependent on the objective function, so determining the appropriate objective function is key to finding the global optimal solution. It is hoped that the body vertical acceleration, pitch angle acceleration and side inclination acceleration, as well as four suspension dynamic travel and four tire dynamic displacement indicators can be optimized. Taking the performance indicators of passive suspension as a reference, the optimization objectives as shown in Formula (19) are designed [28,29]:

$$f_i = \frac{RMS_{semi-active-i}}{RMS_{passive-i}} \quad (i = 1, 2, 3 \dots 10)$$
(19)

where  $RMS_{semi-active-i} (i = 1, 2, 3 \dots 10)$  is the square mean root value of 10 performance indicators output by semi-active suspension, and is the square mean root value of 10 performance indicators output by passive suspension corresponding to the output of semi-active suspension. The 10 performance indicators are vertical acceleration of the body, pitch angle

acceleration, four suspension dynamic travel variables and four tire dynamic displacement variables. In order to achieve better optimization results, a penalty function is given as in Equation (20):

At that time, if  $RMS_{semi-active-i} > RMS_{passive-i}$  ( $i = 1, 2, 3 \dots 10$ ), then:

$$f_i = \sum_{i=1}^{10} \frac{RMS_{semi-active-i}}{RMS_{passive-i}} + 10(i = 1, 2, 3 \dots 10) \quad (20)$$

Therefore  $q_j, j = 1, 2, 3 \dots 12$ ;  $K_p, K_i, K_d, \lambda, \mu$  are the design variables, and  $f_i$  are the optimization objectives; the expression is as follows:

$$\begin{cases} find \left\{ \begin{array}{l} q_j, j = 1, 2, 3 \dots 12 \\ K_p, K_i, K_d, \lambda, \mu \end{array} \right. \\ \min(f_i, i = 1, 2, 3 \dots 10) \\ s.t \left\{ \begin{array}{l} 10^{-4} < q_j < 10^6, j = 1, 2, 3 \dots 12 \\ 0 < K_p, K_i, K_d < 5000, 0 < \lambda, \mu < 2 \end{array} \right. \end{cases} \quad (21)$$

Simulink was used to build a simulation model of the control system, in order to display the established mathematical model more clearly and reflect the core work done. An M-file was written, and part of the pseudo-code is as follows:

for

```
%%Set the parameters and matrix in the state space expression: A, B, C, D, E
%%Define the variables in the LQR controller and find the gain K
q = diag([x(1), x(2), x(3), x(4), x(5), x(6), x(7), x(8), x(9), x(10), x(11)]);
r = diag([x(12), x(12), x(12), x(12)]);
Q = C' * q * C;
N = C' * q * D;
R = r + D' * q * D;
K = lqr(A, B, Q, R, N)
%%Define variables in the fractional order PIλDμ controller
Ki = x(13);
λ = x(14);
Kp = x(15);
Kd = x(16);
μ = x(13);
%%Import the parameters Kp, Ki and Kd, λ and μ, gain K into the MATLAB workspace
assignin('base', 'Kp', Kp);
assignin('base', 'Ki', Ki);
assignin('base', 'Kd', Kd);
assignin('base', 'λ', λ);
assignin('base', 'μ', μ);
assignin('base', 'K', K);
%%The semi-active suspension simulation model is invoked for simulation
[tout,xout,y1,y2,y3,y4,y5,y6,y7,y8,y9,y10] = sim('model.mdl',[0,10]);
```

end

The above pseudocode is mainly divided into two parts: one is to solve the parameter  $K$  in the LQR controller by using the Rikati equation such as Formula (15), and the other is to determine the parameters  $K_p, K_i, K_d, \lambda$  and  $\mu$  in the fractional order  $PI^\lambda D^\mu$  controller. According to the corresponding algorithm, the optimal parameters of the controller are determined and brought to the simulation model (Figure 5) to run the simulation.

#### 4.2. NSGA-II Algorithm to Find the Parameters of the Controller

For multi-objective optimization problems, various optimization objectives may conflict with each other and need to be weighed among various indicators, so it is necessary to select a suitable multi-objective optimization algorithm for optimization. Genetic algorithm is a group search algorithm that simulates the biological evolution process, constantly searching and comparing the best solution and eliminating the difference solution. The standard genetic algorithm will discard the last individual in the iteration process. As a classic modern genetic algorithm, the NSGA-II algorithm uses the elite retention strategy to better retain the elite individual, and solves the problem that the last generation of individuals in the standard genetic algorithm is discarded in the iteration process [30]. In addition, this algorithm reduces the computational complexity of the algorithm by using a fast non-dominated sorting method. The traditional genetic algorithm is mainly used to solve single-objective optimization problems, and the NSGA-II algorithm expands the application scope of traditional genetic algorithms, especially suitable for solving multi-objective optimization problems. The advantages of the NSGA-II algorithm are mainly reflected in three aspects: (1) Elite retention strategy. Elite retention strategies expand the scope of screening when producing the next generation of individuals by mixing parent and child individuals into new groups. The elite retention strategy ensures that excellent individuals can have a greater probability of being retained, ensuring that the population is genetically better after continuous reproduction; (2) Non-dominated sorting. NSGA-II generates a set of non-dominated solution sets by ranking individuals according to their domination by other individuals, which enables NSGA-II to optimize multiple objective functions at the same time and obtain a series of optimal solutions; (3) Crowding sorting. The NSGA-II algorithm maintains population diversity by adopting the concept of crowding distance, and selects a better solution set based on this. The crowding distance is used to measure the local density of individuals in the solution space, and the distance between individuals is taken into account in the selection, so as to ensure the diversity of solution sets.

The NSGA-II algorithm was chosen to solve the multi-objective problem, and the flow chart of the algorithm is shown in Figure 6.

The NSGA-II algorithm has more operation processes than the traditional genetic algorithm (GA), as shown in part 1 (elite retention strategy) and part 2 (non-dominated sorting and crowding sorting), and more operation processes in step 1 than the first generation of nondominated ranking genetic algorithm (NSGA). The specific operation of the NSGA-II algorithm is as follows. Firstly, the initial population of a certain size is randomly generated, and the first generation population is obtained through the selection, crossover and mutation operations of the genetic algorithm after non-dominating sorting. Secondly, starting from the second generation, the parent population and the offspring population are merged, and rapid nondominant ranking is carried out. The individuals in the high-ranking non-dominant layer are retained as the parent generation as the population elite, and the individuals in the low-ranking dominant layer are directly eliminated. The crowding of the individuals in each non-dominant layer is then calculated, and the appropriate individuals are selected to form a new parent population according to the non-dominant relationship and the crowding of the individual. Finally, new offspring populations are generated through the basic operation of genetic algorithms; this process continues until the running conditions for the end of the program are met.

In Figure 6, Part 1 represents the elite retention strategy of the population, and Part 2 represents the non-dominant sorting process and the crowded sorting process of the population.

A more detailed introduction to the NSGA-II algorithm is shown in Figure 7:

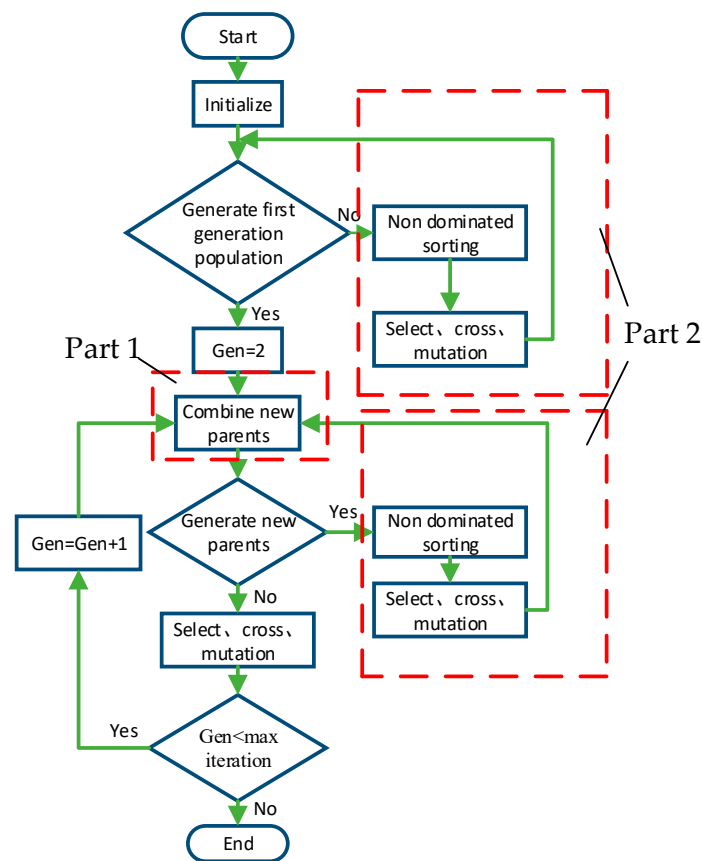


Figure 6. Flowchart of NSGA-II optimization algorithm.

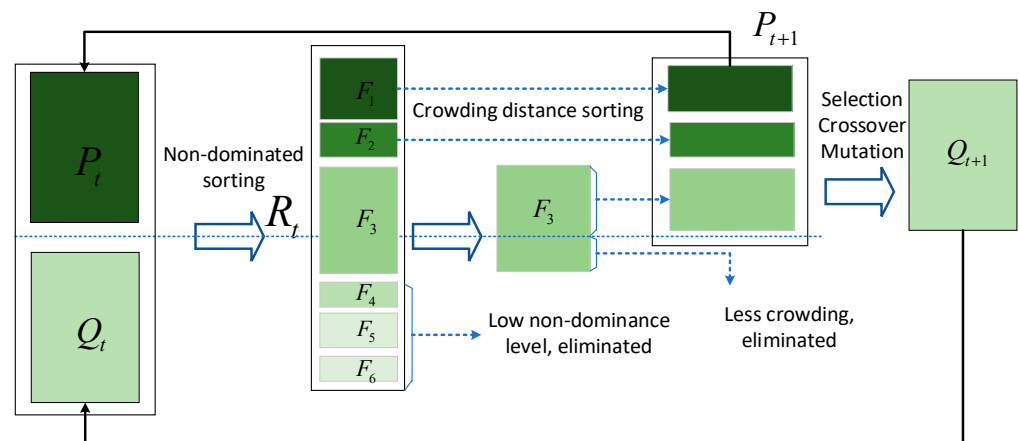


Figure 7. Schematic of the NSGA-II algorithm.

As shown in Figure 7, the population reproduction process  $P_t$  represents the parent population,  $Q_t$  represents the offspring population, and  $R_t$  is the new population produced after the merger of the parent and offspring populations. The population size is set to  $N$ , and the specific steps in Figure 7 are described as follows:

Step 1: Merge the parent and offspring populations into a new population  $R_t$ ; non-dominate the new population  $R_t$  according to the dominance relationship between individuals; and divide the sorted population  $R_t$  into multiple Pareto levels (here the population is divided into 6 Pareto levels:  $F_1, F_2, \dots, F_6$ ).

Step 2: First put the nondominant individual ( $F_1$ ) with a Pareto level of  $F_1$  into a new parent set  $P_{t+1}$  (the darkest color set in the figure), then put the individual with a Pareto

level of F2 into the new parent set  $P_{t+1}$  (as shown in the set with the next color depth in the figure), and so on.

Step 3: If all individuals with grades F1 and F2 are placed in the new parent set  $P_{t+1}$ , and the number of individuals in the set  $P_{t+1}$  is less than the population size  $N$ , the crowding of all individuals at level F3 is calculated and all individuals are arranged in descending order according to crowding, and then all individuals with grades greater than F3 (F4, F5, F6) are eliminated.

Step 4: Place the individuals at level F3 into the new parent set one by one in the order arranged in step 2 until the number of individuals in the parent set equals the population size  $N$ , and the remaining individuals are eliminated.

The concept of dominance can be expressed in Figure 8:

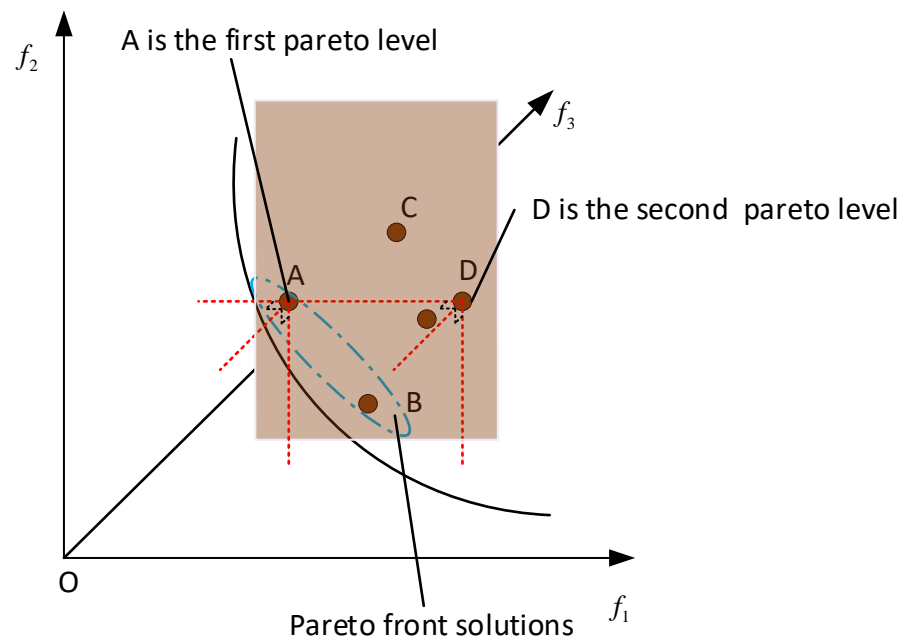


Figure 8. Domination concept schematic.

Figure 8 is a schematic diagram of the dominant concept of the NSGA-II algorithm, in the three-dimensional spatial solution consisting of three objective functions ( $f_1, f_2, f_3$ ); the best solution is that which makes the 3 objective functions  $f_1, f_2, f_3$  smallest in the Pareto frontier. As shown in Figure 6, the four points A, B, C, D are on the same plane, and the plane ABCD and the plane  $f_1o f_2$  are parallel. The distance from point A and point D to plane  $f_1o f_3$  and plane  $f_1o f_2$  is equal, but the distance from point A to plane  $f_2o f_3$  is less than the distance from point D to plane  $f_2o f_3$ . At this time, the non-dominated level of solution A is higher than solution D. A is the non-dominated solution, and D is the dominated solution, but here, solution A dominates solution D; thus, it can be understood that solution A is better than solution D, and in the process of population change, individual A will be retained, while individual D will be eliminated.

The crowding comparison operator is used to compare among quickly ranked peers, thus placing individuals in the quasi-Pareto realm. When the objective function obtained is  $s$ , the crowding distance can be expressed as:

$$i_d = \sum_{j=1}^s \left( \left| f_j^{i+1} - f_j^{i-1} \right| \right) \tag{22}$$

In Formula (22),  $i_d$  represents the crowding distance of point  $i$ ,  $f_j^{i-1}$  represents the  $j$  objective function value of point  $i - 1$ , and  $f_j^{i+1}$  represents the  $j$  objective function value of point  $i + 1$ .

The concept of crowding can be expressed in Figure 9.

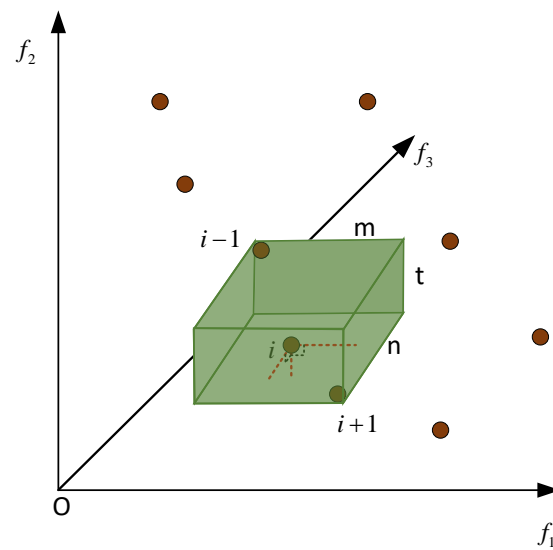


**Figure 9.** Crowding concept diagram.

Figure 9 is a schematic diagram of the congestion concept of the NSGA-II algorithm. In a three-dimensional spatial solution composed of three objective functions  $f_1, f_2, f_3$ , the spatial distance between point  $i$  and the adjacent two points  $i - 1, i + 1$  can be represented by  $m + n + t$ , by the sum of the length  $n$ , width  $m$ , and height  $t$  of the cuboid composed of these three points. In the Pareto frontier solution, the larger the spatial distance of point  $i$ , the better the solution, and point  $i$  is in the highest non-dominant position and belongs to the best solution among all solutions [31].

The optimal solution of the multi-objective optimization problem is the solution of individual  $i$  with the largest crowding degree distance in the front solution.

The main parameters of NSGA-II algorithm are shown in Table 1.

**Table 1.** Main parameters of NSGA-II algorithm.

Parameters	Value
Population number	100
Crossover probability	0.9
Variation distribution indicator	20
Number of iterations	600
Maximum number of failed runs	5
Fail to run penalty values	1000

After 600 iterations, the Pareto solution is obtained, where  $f_i (i = 1, 2, 3, \dots, 10)$  is the  $i$  optimization objective. The solutions in three-dimensional space between each of the three optimization objectives and the projection in three planes are obtained as shown in Figure 10.

$f_1$  is used to represent the vertical acceleration indicator of the body;  $f_2$  is used to represent the pitch angle acceleration indicator;  $f_3, f_4, f_5$  and  $f_6$  are used to represent the four suspension dynamic travel indicators;  $f_7, f_8, f_9$  and  $f_{10}$  are used to represent the four tire dynamic displacement indicators; (a), (b), (c), (d) represent the Pareto solution of each of the three optimization indicators and the projection of these solutions in the spatial Cartesian coordinate system; and the projection represents the local optimal solution between the corresponding two indicators. The local optimal solution between each of the three performance indicators in Figure 10 is circled by the red dashed line as the Pareto leading solution, and the global optimal solution is obtained in the local optimal solution.

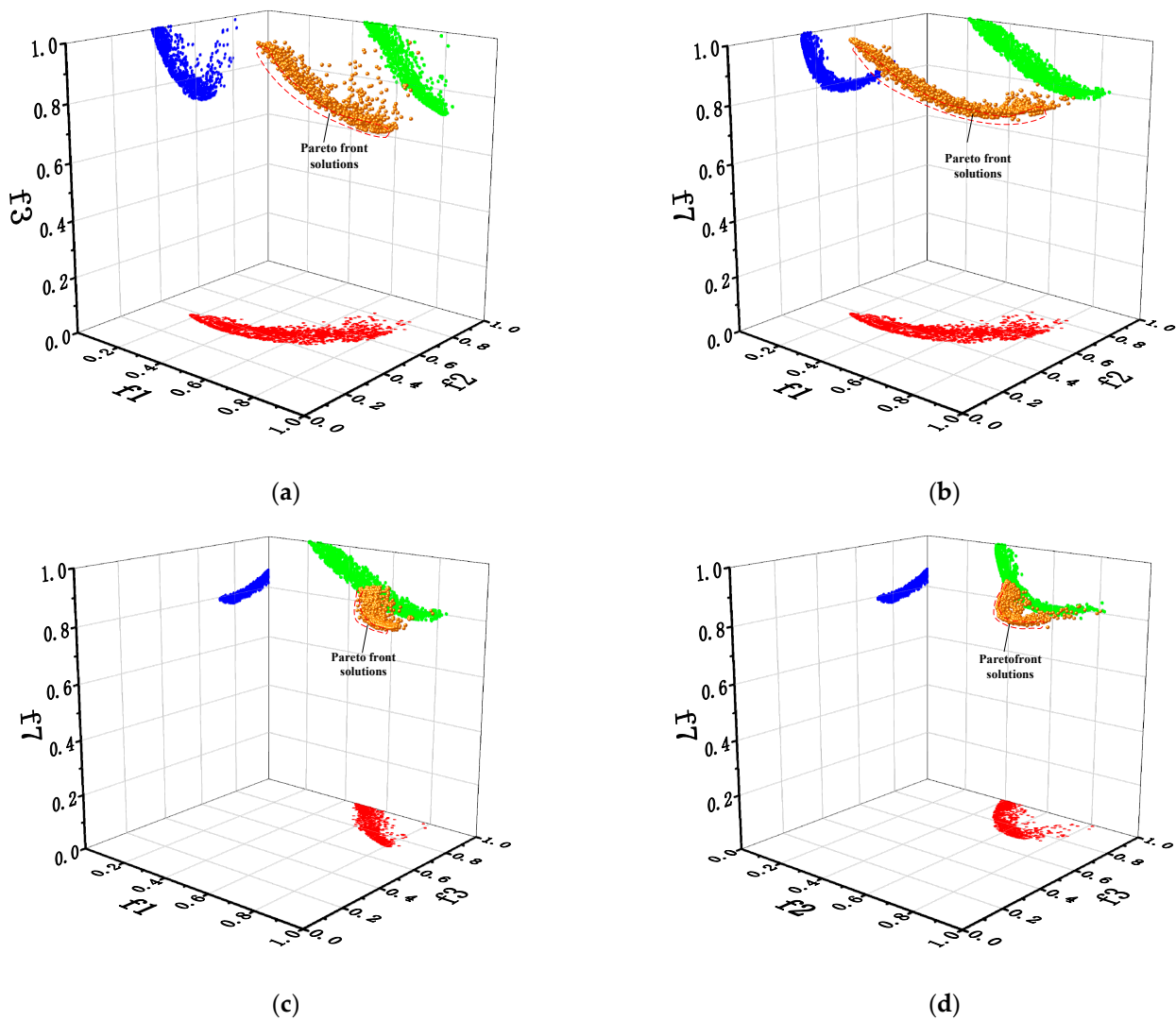


**Figure 10.** (a) Pareto solution of objective functions  $f_1, f_2, f_3$ ; (b) Pareto solution of objective functions  $f_1, f_2, f_7$ ; (c) Pareto solution of objective functions  $f_1, f_3, f_7$ ; (d) Pareto solutions of objective functions  $f_2, f_3, f_7$ .

From Figure 10, it can be seen that the solutions between each of the three objective functions are centrally distributed in a certain region of three-dimensional space, and Pareto frontier solutions exist in all of them, indicating that all objective functions are optimized. Among the frontier solutions in the 10-dimensional space composed of 10 objective functions, a solution with the largest crowding degree distance can be obtained as the global optimal solution.

The 12 weight variables are obtained as follows:

$$\begin{cases} q_1 = 80003.49, q_2 = 1000000.00, q_3 = 398530.00 \\ q_4 = 1000000.00, q_5 = 920000.00, q_6 = 760000.00 \\ q_7 = 820000.00, q_8 = 962489.99, q_9 = 880000.00 \\ q_{10} = 877389.99, q_{11} = 460000.00, q_{12} = 1.00 \end{cases}$$

The five parameters of the fractional order  $PI^\lambda D^\mu$  controller are obtained as follows:

$$\begin{cases} K_p = 1.098 \\ K_i = 2944.466 \\ \lambda = 1.336 \\ K_d = 0.0001 \\ \mu = 1.561 \end{cases}$$

To test the optimized parameters  $K_p$ ,  $K_i$ ,  $K_d$ ,  $\lambda$  and  $\mu$  and whether the stability of the system can be guaranteed, the zero-pole distribution diagram of the transfer function of the closed-loop system (fractional order  $PI^\lambda D^\mu$  closed-loop control part:  $r(t) = 0$  as the expected value input,  $y(t) = \ddot{z}_s(t)$  as the output, as shown in Figure 5) is obtained after the identification of the control system by using the system identification toolbox of MATLAB, as shown in Figure 11.

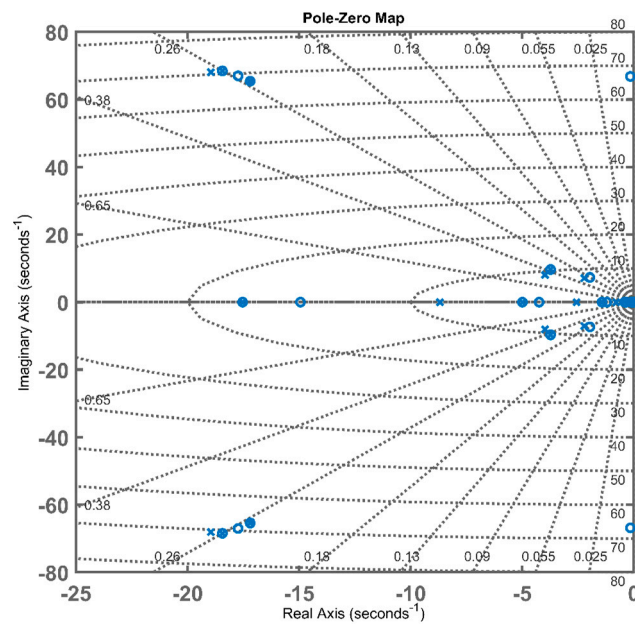


Figure 11. Zero-pole distribution diagram of closed-loop system.

As can be seen from Figure 11, the zeros and poles of the closed-loop system are completely distributed in the left half of the complex plane, indicating that the optimized parameter  $K_p$ ,  $K_i$ ,  $K_d$ ,  $\lambda$  and  $\mu$  can ensure system stability.

## 5. Model Simulation and Result Analysis

### 5.1. Model Simulation

In order to highlight the control effect of fractional order  $PI^\lambda D^\mu$ -LQR composite control, the simulation results are compared with those of passive suspension, the fractional order  $PI^\lambda D^\mu$  control and the LQR control. The simulation time is 10 s, the simulation step length range is [0.01, 0.001], the fixed speed is 20 m/s, the road grade is branch road, and the value range of the road unevenness coefficient under this road condition is  $5 \times 10^{-7} \sim 3 \times 10^{-5}$ , with a mean of  $5 \times 10^{-6}$ . The time domain curve of each performance indicator is obtained, and the power spectral density curve of each performance indicator can be obtained by Fourier transform of the output time domain curve. The range of horizontal coordinates is 0–5 s. Figure 12 shows the time domain curve of each performance indicator:

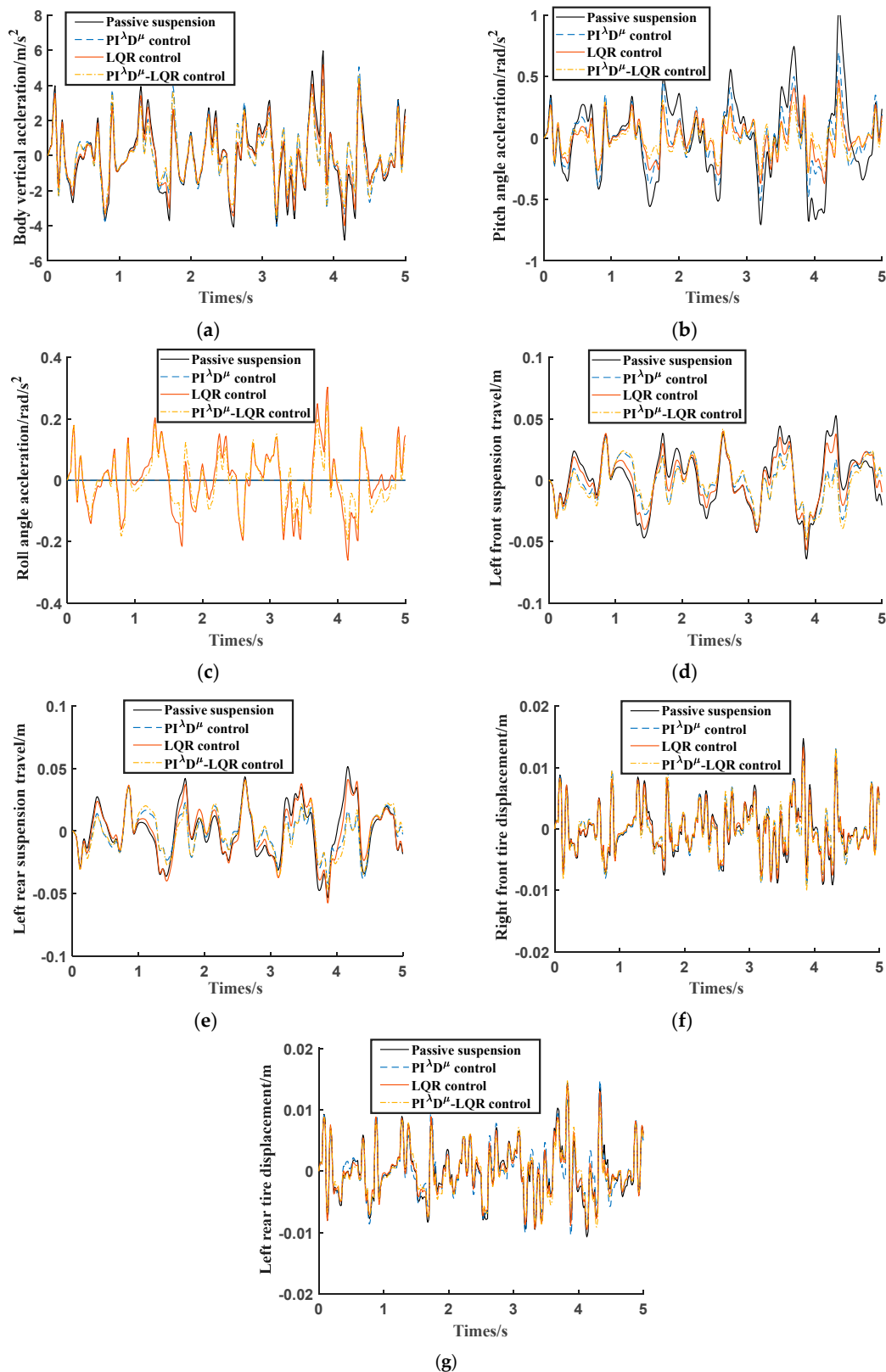


**Figure 12.** (a) Time domain curve of vehicle body vertical acceleration; (b) time domain curve of pitch angle acceleration; (c) time domain curve of roll angle acceleration; (d) time domain curve of left front suspension dynamic travel; (e) time domain curve of left rear suspension dynamic travel; (f) time domain curve of right front tire dynamic displacement; (g) time domain curve of left rear tire dynamic displacement.

As can be seen from Figure 12, the effect of fractious-order  $PI^\lambda D^\mu$ -LQR composite control is more obvious than that obtained by passive suspension, fractious-order  $PI^\lambda D^\mu$  control alone and LQR control alone. The peak value of the output performance indicator curve of the fractional order  $PI^\lambda D^\mu$ -LQR control significantly decreases, but the roll angle acceleration slightly worsens.

Figure 13 shows the power spectral density curves corresponding to the time-domain curves of each performance indicator. Considering that the excitation of the branch road generally does not exceed 10 Hz, the frequency range of the horizontal coordinate is 0–15 Hz.

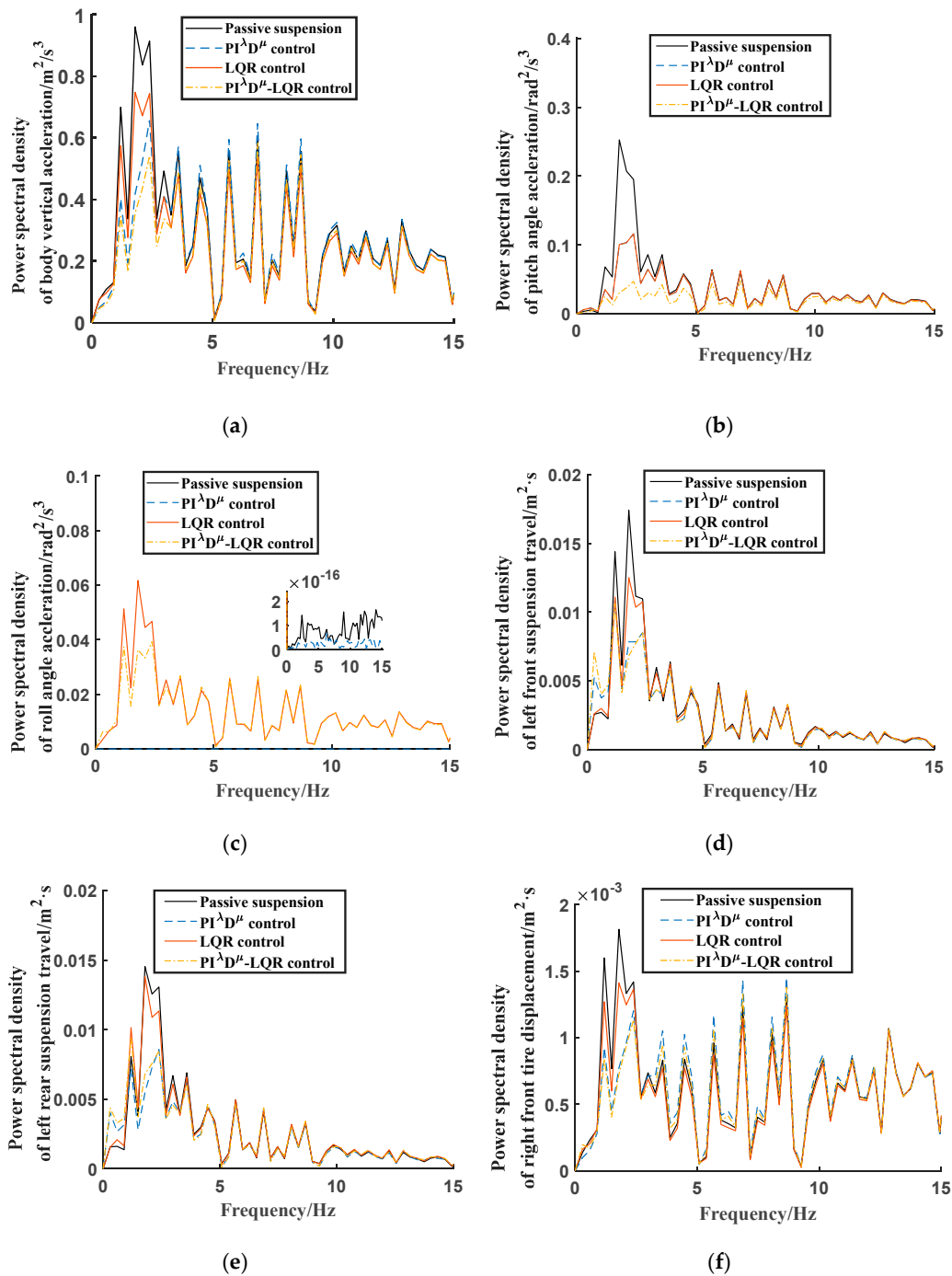
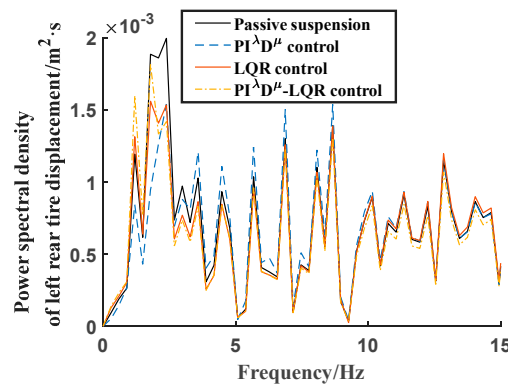


Figure 13. Cont.



(g)

**Figure 13.** (a) Power spectral density curve of the vertical acceleration of the vehicle body; (b) power spectral density curve of pitch angle acceleration; (c) power spectral density curve of roll angle acceleration; (d) power spectral density curve of left front suspension dynamic travel; (e) power spectral density curve of left rear suspension dynamic travel; (f) power spectral density curve of right front tire dynamic displacement; (g) power spectral density curve of the left rear tire dynamic displacement.

As can be seen from Figure 13, compared with passive suspension, the fractional order  $PI^\lambda D^\mu$  control and the LQR control, after adopting the fractional order  $PI^\lambda D^\mu$ -LQR composite control, the power spectral density of body vertical acceleration, pitch angle acceleration, suspension dynamic travel and tire dynamic displacement significantly decreases in the frequency range of 0–5 Hz, while the change is not obvious in the frequency range of 5–15 Hz. This indicates that after active control, the actuator can well suppress the low-frequency impact from the road surface, but the suppression effect on the high-frequency impact is not obvious.

5.2. Results Analysis

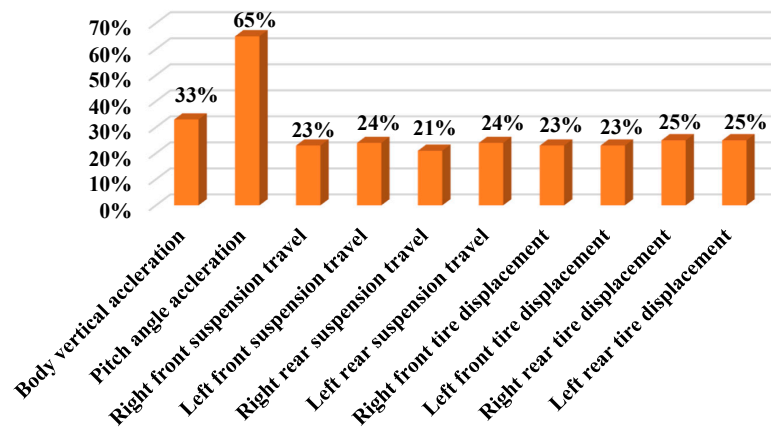
5.2.1. Improvement of Performance Indicators

In order to more clearly reflect the advantages of the fractional order  $PI^\lambda D^\mu$ -LQR composite control, the time-domain curves of each performance indicator are squared and the average root values are shown in Table 2.

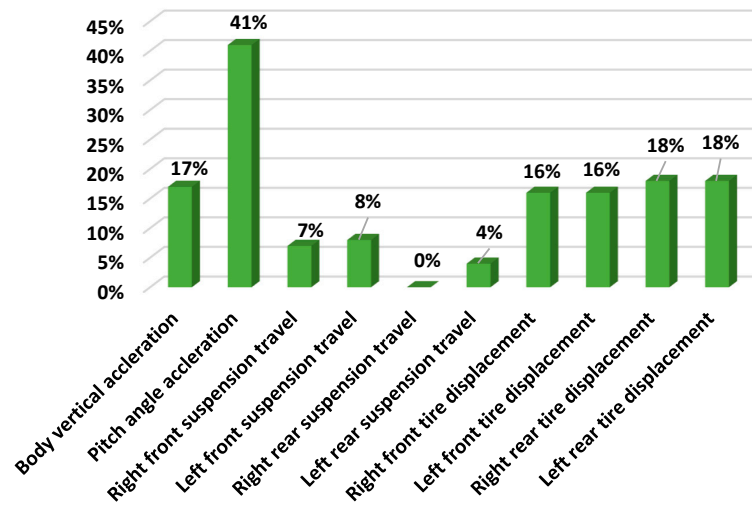
**Table 2.** Average root value of each performance indicator.

Indicators	Passive	$PI^\lambda D^\mu$ Control	LQR Control	$PI^\lambda D^\mu$ -LQR Control
$\ddot{z}_s$	2.0187	1.6297	1.4983	1.3602
$\ddot{\varphi}$	0.3237	0.1945	0.1391	0.1149
$\ddot{\theta}$	$3.1 \times 10^{-15}$	$1.1 \times 10^{-16}$	$9.3 \times 10^{-6}$	$4.6 \times 10^{-6}$
$z_{swf1}$	0.0219	0.0182	0.0173	0.0170
$z_{swf2}$	0.0219	0.0182	0.0175	0.0168
$z_{swr1}$	0.0201	0.0159	0.0171	0.0159
$z_{swr2}$	0.0201	0.0159	0.0180	0.0153
$z_{qwf1}$	0.0048	0.0044	0.0037	0.0037
$z_{qwf2}$	0.0048	0.0044	0.0037	0.0037
$z_{qwr1}$	0.0052	0.0047	0.0039	0.0039
$z_{qwr2}$	0.0052	0.0047	0.0041	0.0040

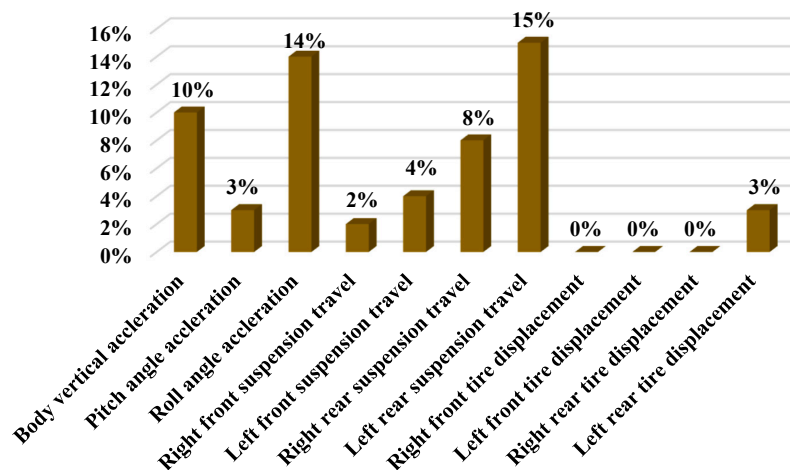
As can be seen from Table 2, after the fractional order  $PI^\lambda D^\mu$ -LQR composite control is adopted, compared with the passive suspension, the other performance indicators are greatly optimized except for the slight deterioration of the roll angle acceleration. In order to display the improved condition of the optimized performance indicators more directly, a bar chart of the improvement of the indicators is shown in Figure 14:



(a)



(b)



(c)

**Figure 14.** (a) Improvement of performance indicators of the fractional order  $PI^{\lambda}D^{\mu}$ -LQR control compared with passive suspension; (b) performance improvement of the fractional order  $PI^{\lambda}D^{\mu}$ -LQR control compared with fractional order  $PI^{\lambda}D^{\mu}$  control; (c) fractional order  $PI^{\lambda}D^{\mu}$ -LQR control compared with the LQR control.

By analyzing the data, it can be found that the control effect of the fractional order  $PI^\lambda D^\mu$ -LQR composite control is remarkable. All performance indicators are optimized to the greatest extent on the basis of the fractional order  $PI^\lambda D^\mu$  control and the LQR control.

### 5.2.2. Influence of Actuator Output Force on Roll Angle Acceleration

By analyzing Formula (3), it can be found that while the left and right suspension stiffness are the same, the roll angle acceleration indicator is only related to the dynamic travel of the four suspensions and the regulating force of the four actuators. Combined with Table 1, it is noted that the dynamic travel of the left and right suspension of the passive suspension is exactly the same, and the left and right roll torque is balanced, so the square mean root value of the roll angle acceleration of the passive suspension is very small. After active control is adopted, when the dynamic travel of left and right suspension is not much different, the acceleration indicator of side inclination is mainly affected by the adjustment force of four actuators.

When the weighting coefficients of the four actuators in the matrix R of Formula (17) are the same, the regulating force output by the four actuators is the balanced force; when the weighting coefficients of the four actuators are different, the regulating force output is the unbalanced force. The adjusting force output by the actuator in two cases is shown in Figures 15 and 16, respectively:

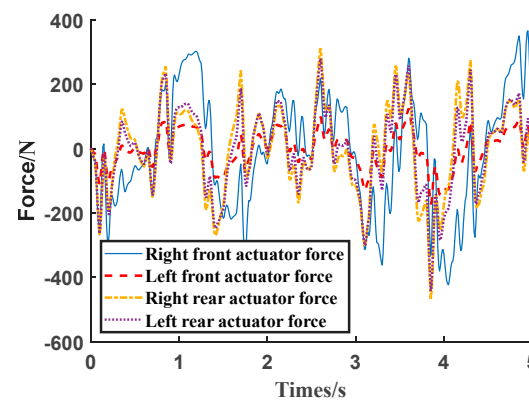


Figure 15. Unbalanced regulating force output by 4 actuators.

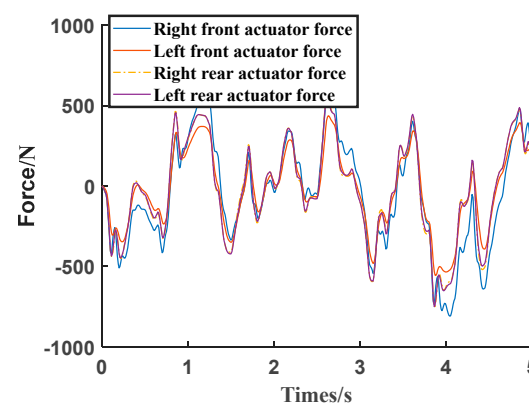


Figure 16. Balanced regulating force output by 4 actuators.

In order to visually compare the influence of the adjusting force output by the four actuators on the roll angle acceleration, the time-domain curve of the roll angle acceleration is obtained as shown in Figure 17:

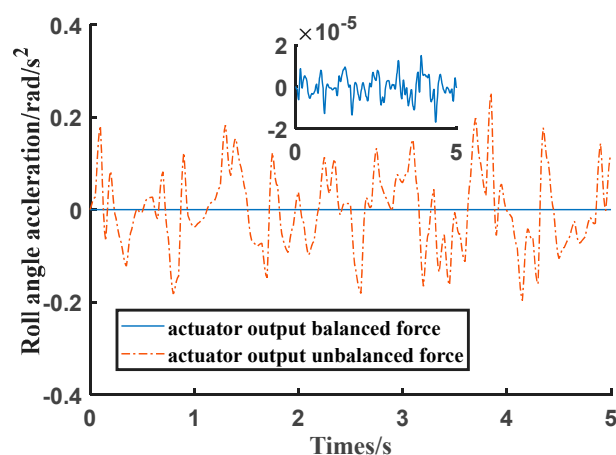


Figure 17. Influence of adjusting force of the actuator on roll angle acceleration.

Obviously, the balanced adjustment force output by four actuators can more effectively restrain the roll of the car body and improve the stability of the car body.

## 6. Conclusions

This paper introduces theoretical research on the analysis, modeling and simulation of semi-active suspension control systems of vehicles. Firstly, through the force analysis of the semi-active suspension dynamic model of the whole vehicle, the differential equation of motion of the whole vehicle in the direction of seven degrees of freedom is derived, and it is expressed in the form of state space. Secondly, according to the fractional  $PI^\lambda D^\mu$  control theory and LQR control theory, the fractional  $PI^\lambda D^\mu$ -LQR controller was designed, and the simulation model of the fractional  $PI^\lambda D^\mu$ -LQR control system was built by MATLAB/simulink. A non-dominant ranking genetic algorithm (NSGA-II) is then introduced, and the concepts of dominance, crowding and elite retention strategy of the NSGA-II algorithm are explained in detail. Because of the advantages embodied by the NSGA-II algorithm, it was used to optimize the weighting coefficient of 12 performance indicators and parameters  $K_p$ ,  $K_i$ ,  $K_d$ ,  $\lambda$  and  $\mu$  in the fractional order  $PI^\lambda D^\mu$ -LQR controller. Finally, the parameters after tuning are brought into the controller for simulation, and at the same time, in order to reflect the advantages of the proposed fractional  $PI^\lambda D^\mu$ -LQR control method, compared with passive suspension, the fractional order  $PI^\lambda D^\mu$  control and the LQR control, the comparison results show that the fractional  $PI^\lambda D^\mu$ -LQR compound control is better than the fractional order  $PI^\lambda D^\mu$  control and LQR control, and the performance indicators are improved to the greatest extent. Through simulation, it is found that the balanced adjustment force output by four actuators can effectively restrain the body roll. The fractional order  $PI^\lambda D^\mu$  control and the LQR control are combined to give full play to the advantages of the two control methods and improve the control effect.

**Author Contributions:** Conceptualization, J.G. and H.L.; methodology, J.G. and H.L.; software, J.G. and H.L.; validation, J.G. and H.L.; formal analysis, J.G. and H.L.; investigation, J.G. and H.L.; resources, J.G. and H.L.; data curation, H.L.; writing—original draft preparation, J.G. and H.L.; writing—review and editing, J.G.; visualization, J.G. and H.L.; supervision, J.G.; project administration, J.G.; funding acquisition, J.G. All authors have read and agreed to the published version of the manuscript.

**Funding:** This work was supported by National Natural Science Foundation of China (Grant No. 51965026).

**Data Availability Statement:** Not applicable.

**Conflicts of Interest:** The authors declare no conflict of interest.

## References

1. Lee, D.; Jin, S.; Lee, C. Deep Reinforcement Learning of Semi-Active Suspension Controller for Vehicle Ride Comfort. *IEEE Trans. Veh. Technol.* **2023**, *72*, 327–339. [\[CrossRef\]](#)
2. Li, Z.X.; Pan, S.J.; Zhu, Y.; He, B.; Xu, Y.C. Semi-active Suspension Control for Intelligent Vehicles Based on State Feedback and Preview Feedforward. *Qiche Gongcheng/Automot. Eng.* **2023**, *45*, 735–745.
3. Ahn, D.-V.; Kim, K.; Oh, J.; Seo, J.; Lee, J.W.; Park, Y.-J. Optimal Control of Semi-Active Suspension for Agricultural Tractors Using Linear Quadratic Gaussian Control. *Sensors* **2023**, *23*, 6474. [\[CrossRef\]](#) [\[PubMed\]](#)
4. Basargan, H.; Mihály, A.; Gáspár, P.; Sename, O. Cloud-based adaptive semi-active suspension control for improving driving comfort and road holding. *IFAC-Pap.* **2022**, *55*, 89–94. [\[CrossRef\]](#)
5. Yang, P.; Ge, Y.; Liu, H.; Zeng, X.; Li, C. Joint Control of Semi-active Suspension Based on CDC Shock Absorber. In Proceedings of the 2022 41st Chinese Control Conference (CCC), Hefei, China, 25–27 July 2022; pp. 5396–5401. [\[CrossRef\]](#)
6. Gampa, S.R.; Mangipudi, S.K.; Jasthi, K.; Goli, P.; Das, D.; Balas, V.E. Pareto Optimality Based PID Controller Design for Vehicle Active Suspension System Using Grasshopper Optimization Algorithm. *J. Electr. Syst. Inf. Technol.* **2022**, *9*, 9–24. [\[CrossRef\]](#)
7. Zhao, W.P.; Gu, L.; Dong, M.M. Application of Artificial Fish Swarm Algorithm in LQR Control for Active Suspension. *Asian Control. Conf. Proc.* **2022**, *3*, 2406–2409.
8. Munawwarah, S.; Yakub, F. Control Analysis of Vehicle Ride Comfort through Integrated Control Devices on the Quarter and Half Car Active Suspension Systems. *Proc. Inst. Mech. Eng. Part D J. Automob. Eng.* **2021**, *235*, 1256–1268. [\[CrossRef\]](#)
9. Joshi, M.; Sharma, G. Load Frequency Control of Hydro-Hydro Power System using Fuzzy-PSO-PID with Application of UC and RFB. *Electr. Power Compon. Syst.* **2023**, *12*, 1156–1170. [\[CrossRef\]](#)
10. Rashki, M.; Faes, M.G. No-Free-Lunch Theorems for Reliability Analysis. *ASCE-ASME J. Risk Uncertain. Eng. Syst. Part A Civ. Eng.* **2023**, *9*, 04023019. [\[CrossRef\]](#)
11. Sharma, K.; Cerezo, M.; Holmes, Z.; Cincio, L.; Sornborger, A.; Coles, P.J. Reformulation of the No-Free-Lunch Theorem for Entangled Datasets. *Phys. Rev. Lett.* **2022**, *128*, 070501. [\[CrossRef\]](#)
12. Orosz, T.; Rassölkin, A.; Kallaste, A.; Arsénio, P.; Pánek, D.; Kaska, J.; Karban, P. Robust Design Optimization and Emerging Technologies for Electrical Machines: Challenges and Open Problems. *Appl. Sci.* **2020**, *10*, 6653. [\[CrossRef\]](#)
13. Wang, D. Multi-Objective Lightweight Optimization of Parameterized Suspension Components Based on NSGA-II Algorithm Coupling with Surrogate Model. *Machines* **2021**, *9*, 107. [\[CrossRef\]](#)
14. Gheibollahi, H.; Masih-Tehrani, M. A multi-objective optimization method based on NSGA-II algorithm and entropy weighted TOPSIS for fuzzy active seat suspension of articulated truck semi-trailer. *Proc. Inst. Mech. Eng. Part C J. Mech. Eng. Sci.* **2023**, *237*, 3809–3826. [\[CrossRef\]](#)
15. Nagarkar, M.; Bhalerao, Y.; Sashikumar, S.; Hase, V.; Navthar, R.; Zaware, R.; Thakur, A.; Wable, A.; Ashtekar, J.; Surner, N. Multi-objective optimization and experimental investigation of quarter car suspension system. *Int. J. Dynam. Control* **2023**. [\[CrossRef\]](#)
16. Laldingliana, J.; Biswas, P.K. Artificial Intelligence Based Fractional Order  $PI^{\lambda}D^{\mu}$  Control Strategy for Active Magnetic Bearing. *J. Electr. Eng. Technol.* **2022**, *17*, 3389–3398.
17. Rahmani, M.; Redkar, S. Data-driven Koopman fractional order  $PI^{\lambda}D^{\mu}$  control of a MEMS gyroscope using bat algorithm. *Neural Comput. Appl.* **2023**, *35*, 9831–9840. [\[CrossRef\]](#)
18. Na, J.; Huang, Y.; Pei, Q.; Wu, X.; Gao, G.; Li, G.. Active Suspension Control of Full-Car Systems without Function Approximation. *IEEE/ASME Trans. Mechatron.* **2020**, *25*, 779–791. [\[CrossRef\]](#)
19. Yu, M.; Cheng, C.; Evangelou, S.A.; Dini, D. Series Active Variable Geometry Suspension: Full-Car Prototyping and Road Testing. *IEEE/ASME Trans. Mechatron.* **2022**, *27*, 1332–1334. [\[CrossRef\]](#)
20. Yu, F.; Lin, Y. *Automotive System Dynamics*, 2nd ed.; China Machine Press: Beijing, China, 2016.
21. Cui, S.M. *Automotive System Dynamics and Simulation*; Peking University Press: Beijing, China, 2014.
22. Liu, Z.; Yuan, X.; Huang, G.; Tan, W.; Wang, Y. 3D Gradient Reconstruction-Based Path Planning Method for Autonomous Vehicle with Enhanced Roll Stability. *IEEE Trans. Intell. Transp. Syst.* **2022**, *23*, 20563–20571. [\[CrossRef\]](#)
23. Wang, H.-P.; Zhang, Z.; Li, Q. Coherence of Phase Angle of Harmonic Superposition Components in Time Domain Simulation of Road Roughness for Right and Left Wheel Tracks. *Beijing Ligong Daxue Xuebao/Trans. Beijing Inst. Technol.* **2019**, *39*, 1034–1038.
24. Wang, J.; Lv, K.; Wang, H.; Guo, S.; Wang, J. Research on nonlinear model and fuzzy fractional order  $PI^{\lambda}D^{\mu}$  control of air suspension system. *J. Low Freq. Noise Vib. Act. Control.* **2022**, *41*, 712–731. [\[CrossRef\]](#)
25. Li, J.; Liu, Y.; Shan, C.; Dai, C. Implementation of Simplified Fractional Order  $PI^{\lambda}D^{\mu}$  Controller Based on Modified Oustaloup's Recursive Filter. *J. Shanghai Jiaotong Univ. (Sci.)* **2020**, *15*, 44–50. [\[CrossRef\]](#)
26. Graa, M.; Nejlaoui, M.; Houidi, A.; Affi, Z.; Romdhane, L. Modeling and Control of Rail Vehicle Suspensions: A Comparative Study Based on the Passenger Comfort. *Inst. Mech. Eng.* **2018**, *232*, 260–274. [\[CrossRef\]](#)
27. Zhang, J.Q.; Peng, H.; Zhang, J.W. Parameters Optimization for the Weight Matrices in a Vehicle Suspension LQR Active Control. *J. Vib. Shock.* **2022**, *22*, 214–219.
28. Prasad, V.; Pawaskar, D.N.; Seshu, P. Controller Design and Multi-objective Optimization of Heavy Goods Vehicle Suspension System by Geometry-inspired GA. *Struct. Multidiscip. Optim.* **2021**, *64*, 89–111. [\[CrossRef\]](#)
29. Guan, G.; Yang, Q.; Wang, Y.; Zhou, S.; Zhuang, Z. Parametric design and optimization of SWATH for reduced resistance based on evolutionary algorithm. *J. Mar. Sci. Technol.* **2021**, *26*, 54–70. [\[CrossRef\]](#)

30. Wang, C.Y.; Zhang, Y.Q.; Zhao, W.Z. Multi-objective optimization of a steering system considering steering modality. *Adv. Eng. Softw.* **2018**, *126*, 61–74. [[CrossRef](#)]
31. Gao, W.G.; Lu, L.X.; Wang, Z.Q.; Liu, C.L. Research on heliostat field scheduling scheme of tower solar power Station based on NSGA-II. *Therm. Power Gener.* **2021**, *50*, 94–101.

**Disclaimer/Publisher’s Note:** The statements, opinions and data contained in all publications are solely those of the individual author(s) and contributor(s) and not of MDPI and/or the editor(s). MDPI and/or the editor(s) disclaim responsibility for any injury to people or property resulting from any ideas, methods, instructions or products referred to in the content.